Available online at www.sciencedirect.com
ScienceDirect
Journal of Solid State Chemistry 180 (2007) 1259–1271
JOURNAL OF SOLID STATE CHEMISTRY
www.elsevier.com/locate/jssc

Ionic and electronic transport in $La_2Ti_2SiO_9$-based materials

Y.V. Pivak, V.V. Kharton*, E.N. Naumovich, J.R. Frade, F.M.B. Marques

Department of Ceramics and Glass Engineering, CICECO, University of Aveiro, 3810-193 Aveiro, Portugal

Received 7 December 2006; received in revised form 6 January 2007; accepted 9 January 2007
Available online 3 February 2007

Abstract

The total conductivity of monoclinic $La_2Ti_2SiO_9$ is mixed oxygen-ionic and n-type electronic, and increases on reduction of the oxygen partial pressure down to 10^{-21} atm at 973–1223 K. The substitution of Ti^{4+} with Nb^{5+} decreases both contributions to the conductivity, whilst Pr doping and reducing $p(O_2)$ have opposite effects. The oxygen ion transference numbers of $La_2Ti_2SiO_{9-\delta}$, $LaPrTi_2SiO_{9\pm\delta}$ and $La_2Ti_{1.8}Nb_{0.2}SiO_{9\pm\delta}$ ceramics, measured by the faradaic efficiency and e.m.f. methods, vary in the range 0.15–0.32, increasing when temperature decreases. In air, the activation energies for the ionic and electronic transport are 1.23–1.40 and 1.59–1.74 eV, respectively. Protonic contribution to the conductivity in wet atmospheres becomes significant at temperatures below 1000 K. The experimental data and the results of atomistic computer simulations suggest that the oxygen-ionic and electronic transport is primarily determined by processes involving TiO_6 octahedra. The ionic conduction may occur via both the vacancy and interstitial migration mechanisms, but the former is more favorable energetically and should dominate, at least, in reducing atmospheres. The average thermal expansion coefficients of $La_2Ti_2SiO_9$-based ceramics, calculated from dilatometric data in air, are $(8.7–9.5)\times10^{-6}\,K^{-1}$ at 300–1373 K. The lattice of lanthanum titanate-silicate is almost intolerant with respect to *A*-site deficiency and to doping with lower-valence cations, such as Sr and Fe.

Keywords: Lanthanum titanate-silicate; Oxygen ionic conductivity; n-type electronic transport; Ion transference number; Thermal expansion; Atomistic computer simulations

1. Introduction

Oxygen ion-conducting solid electrolytes are key materials for numerous high-temperature electrochemical devices, such as solid oxide fuel cells (SOFCs) [1,2]. Although possessing a high energy-conversion efficiency, environmental safety and fuel flexibility, the practical application of SOFCs is still limited due to the high cost of the component materials and processing. Development of novel low-cost materials with optimized transport and thermomechanical properties is of vital importance in this field. Recently, considerable attention has been focused on the silicates with apatite-type $A_{10-x}(SiO_4)_6O_{2-\delta}$ [3–9] and cuspidine-type $A_4(Si_2O_7)O_{2-\delta}$ [10,11] structures, where the *A* sublattice comprises rare-earth and/or alkaline-earth cations. The essential features of these Si-containing solid electrolytes are the flexibility of the crystal structure, enabling improvements in transport properties via cation doping, and an important role of the lattice relaxations near diffusing anions [3–11]. Having a relatively high oxygen-ionic conductivity and a moderate thermal expansion [3–11], these may be of a substantial interest when considering the low cost of raw materials and well-developed technologies for SiO_2-based film processing, used in the electronic industry. On the other hand, despite the great number of silicates where similar structural elements are present in the crystal lattice, and significant ionic conduction may thus be expected, literature data on the correlations between silicate structure and transport properties are scarce. Such information is also critical for the developments of suitable SOFC sealants based on glass-ceramics [12–15], another important challenge for SiO_2-containing materials. The glass-ceramic seals applied to separate cathode and anode chambers and to maintain the gas-tightness of the system, should exhibit thermomechanical and chemical stability and good compatibility with other SOFC components. In terms of electrical

*Corresponding author. Fax: +351 234 425300.
E-mail address: kharton@cv.ua.pt (V.V. Kharton).

0022-4596/$ - see front matter © 2007 Elsevier Inc. All rights reserved.
doi:10.1016/j.jssc.2007.01.024

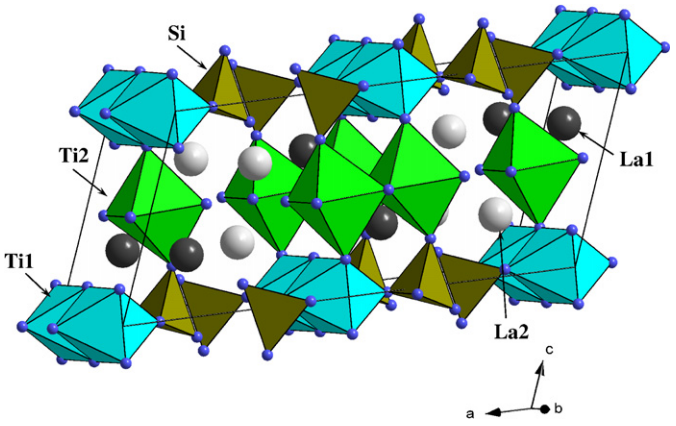

Fig. 1. Crystal structure of $La_2Ti_2SiO_9$.

properties, these glass-ceramics should behave as insulators with total conductivity (σ) lower than 10^{-4} S/cm, in order to avoid parasitic currents decreasing the system efficiency. Due to similar bond energies, the behavior of glassy components is, as a rule, quite similar to that of the parent crystalline phases.

Continuing our research on silicate-based materials for the high-temperature electrochemical applications [8,9], the present work is centered on the study of several compositions within the monoclinic $La_{2-x}A_xTi_{2-y}B_ySiO_{9\pm\delta}$ (A = Pr, Sr, Y; B = Nb, Fe) system. Particular emphasis is given to the phase relationships, total and partial oxygen-ionic conductivities, transference numbers, thermal expansion, and behavior in reducing conditions. The crystal structure of the base compound, $La_2Ti_2SiO_9$ (Fig. 1), includes a network of isolated SiO_4 tetrahedra connected by two types of TiO_6 octahedra. Unlike perovskite-type structures where all octahedra are corner-sharing, the equivalent TiO_6 polyhedra in the $La_2Ti_2SiO_9$ share their edges. Two non-equivalent La sites existing in this structure are located between SiO_4 and TiO_6 units. Also, the lattice comprises relatively large cavities between metal-oxygen polyhedra, which can be occupied by interstitial ions. Possible contributions of oxygen vacancies and interstitials were evaluated incorporating higher- and lower-valence dopants, studying the relationships between transport properties and oxygen partial pressure, and using the atomistic computer simulations.

2. Experimental

Powders of $La_{2-x}A_xTi_{2-y}B_ySiO_{9\pm\delta}$ (A = Pr, Sr, Y; B = Nb, Fe; $x = 0-1$; $y = 0-1$) and $Y_2Ti_2SiO_9$ were prepared from high-purity metal oxides, nitrates and carbonates by the conventional solid-state synthesis route. The reactions were performed at 1173–1473 K for 15–25 h in air, with intermediate re-grinding steps and final ball-milling in ethanol. Then the powders were uniaxially pressed at 100–150 MPa into disks of various thickness; gas-tight ceramics were sintered at 1598–1668 K for 20 h in air. X-ray diffraction (XRD) patterns were collected using a Rigaku D/MAX–B diffractometer (Bragg-Brentano geometry, Cu$K\alpha$ radiation, 2θ angle range 10–100°, step 0.02°, 9 s/step). The structural parameters were refined using the full-profile Rietveld method, employing FullProf software [16]. In the refinement procedure, the scale factor, zero shift and background parameters, lattice constants, atomic coordinates and fractions, isotropic temperature factors, peak profile and texture parameters were taken into account. A Hitachi S-4100 scanning electron microscope (SEM) with a Rontec UHV detection system for the energy-dispersive spectroscopy (EDS) was used for microstructural analysis. Thermal expansion was studied in air using a Linseis L70 dilatometer (heating rate of 3 K/min). Thermogravimetric analysis (TGA) was carried out using a Setaram SetSys 16/18 instrument (flowing dry air, heating/cooling rate of 3 K/min, dwell at 1473 K for 1 h). The temperature dependencies of total conductivity (σ) in flowing air, O_2–Ar and 10%H_2–90%N_2 mixtures were studied by the AC impedance spectroscopy (HP4284A precision LCR meter, 20 Hz–1 MHz); the oxygen partial pressure in the measuring cell was controlled by an yttria-stabilized zirconia (YSZ) oxygen sensor. To estimate possible protonic contributions to the conductivity, the impedance spectra were collected both in dry gas (with the water-vapor partial pressure lower than 10^{-4} atm), and in humidified atmospheres (with $p(H_2O) \approx 0.032$ atm). The oxygen ion transference numbers were determined by the modified electromotive force (EMF) and faradaic efficiency (FE) methods [17,18].

The atomic simulations technique using the GULP software [19] is well known in literature (e.g. [20]). This approach is based on the Born model for ionic solids, where the charge of ions is assigned to their formal oxidation state. The interactions between the ions are formulated in terms of long-range electrostatic (coulombic) forces and short-range Pauli repulsion and van der Waals dispersion, modeled using a standard Buckingham potential:

$$V_{ij} = A_{ij}\exp\left(-\frac{r_{ij}}{\rho_{ij}}\right) - C_{ij}r^{-6}, \quad (1)$$

where A_{ij}, ρ_{ij} and C_{ij} are potential parameters and r_{ij} is the distance between two ions. The polarizability caused by the presence of charged defects in the lattice is taken into account by means of the shell model [21], treating each ion in terms of heavy core (representing the nucleus and core electrons) connected via one harmonic spring to a shell (representing the outer electrons). The defect modelling is performed using a Mott-Littleton approach [22]; the crystal around a defect is partitioned into the inner spherical region with explicit description of atomic relaxations, and the outer region extended to infinity, where the defect-lattice interactions are relatively week and can be treated by approximate quasi-continuum methods. The short-range potential and shell model parameters, including the three-body potential for SiO_4 units, were selected from

Refs. [23–26]. At the first stage of the modelling procedure, the crystal structure of the base composition ($La_2Ti_2SiO_9$) was simulated using the energy minimization procedure. Then the lattices of Pr- and Nb-containing solid solutions with random distribution of the dopant cations were built; the model was verified comparing the final lattice parameters and bond distances to the corresponding structure refinement results. For modeling of the defect migration processes, the $1 \times 3 \times 2$ supercells (space group $P1$) consisting of 648 atoms were constructed; the size was chosen considering lattice relaxations near point defects. These supercells were used to estimate preferential location and the formation energies of isolated point defects, namely oxygen vacancies and interstitials, and to determine the defect migration pathways. Finally, the migration energies for oxygen ions were evaluated from the difference between the saddle-point energy and the energy of the isolated defects formation.

The modelling results showed a significant energetic nonequivalence of many crystallographically-equivalent oxygen positions, depending on their neighborhood. Labeling of atomic positions is necessary in order to distinguish defect configurations and migration pathways with different energies. In the present work, the sites are labeled according to the GULP indexing [19]. As an example, $O4_{248}$ denotes the oxygen anion located in O4 sublattice, position 248.

3. Results and discussion

3.1. Phase relationships and crystal structure

XRD analysis of $La_2Ti_2SiO_9$, $LaPrTi_2SiO_{9+\delta}$ and $La_2Ti_{1.8}Nb_{0.2}SiO_{9+\delta}$ ceramics, annealed at 1170–1270 K and slowly cooled in air in order to achieve equilibrium with atmospheric oxygen, revealed the formation of single monoclinic phases (Fig. 2). No impurity peaks were detected in the XRD patterns. On the contrary, doping with either Sr or Fe leads to phase decomposition (Fig. 3). Analogously, attempts to create A-site cation vacancies in the case of $La_{0.9}PrTi_2SiO_{9-\delta}$ resulted in segregation of ~7.4 wt% of TiO_2, although a small shift in the peak positions of the major phase indicates that a minor cation deficiency is present. Such behavior suggests a very limited tolerance of the $La_2Ti_2SiO_9$ structure with respect to the acceptor-type doping and A-site deficiency, in contrast to the apatite-type silicates [5–9]. Most likely, this is associated with instability of Si^{4+} and Ti^{4+} cations when the oxygen coordination is lower than 4 and 6, respectively. The solubility of donor-type dopants is slightly higher compared to the lower-valence cations, but also limited. For instance, complete decomposition of the $La_2Ti_2SiO_9$-based phase was observed in the case of $La_2TiNbSiO_{9.5}$, where the expected oxygen excess is as low as approximately 5.5%.

Analysis of the XRD pattern of $Y_2Ti_2SiO_9$ ceramics did not reveal formation of a single phase, although the trimounsite-(Y) mineral is known in literature [27]. The major phase obtained in $Y_2Ti_2SiO_9$ was fluorite-type $Y_2Ti_2O_7$; reflexes of $Y_2Si_2O_7$ are also visible (Fig. 3). The structure of trimounsite-(Y) comprises spiral-like chains composed of edge-sharing, strongly distorted TiO_6 octahedra [27]; apparently, these units cannot be formed under ambient conditions.

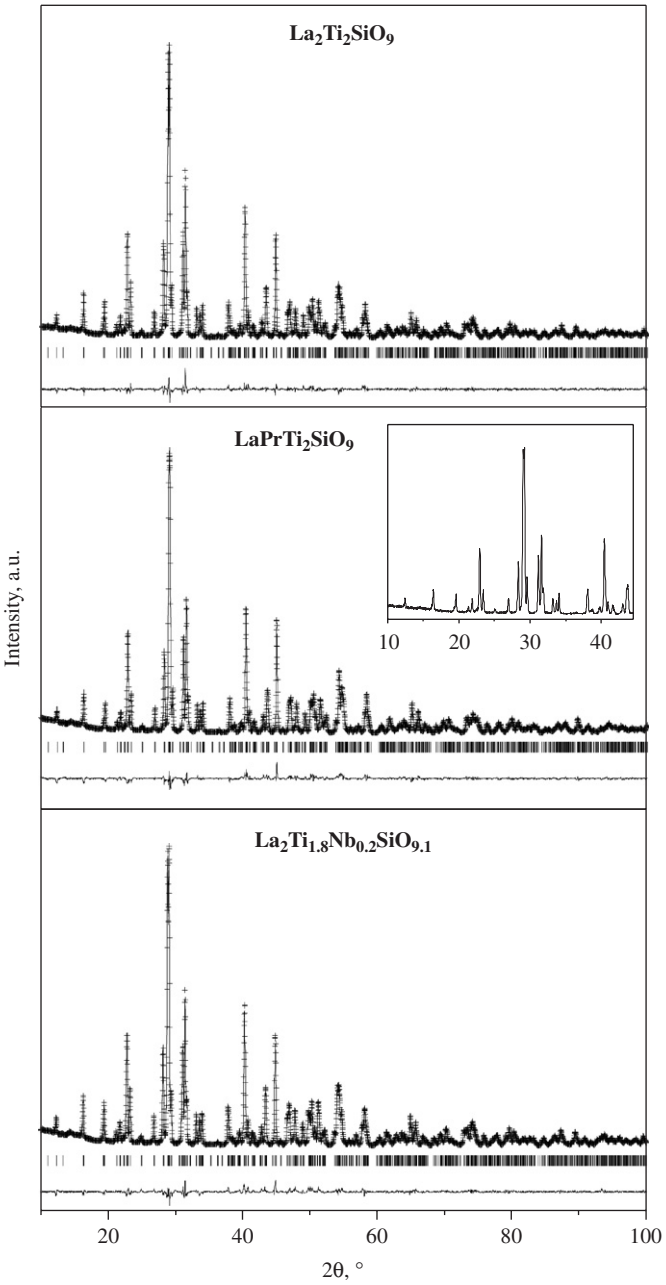

Fig. 2. Experimental, calculated and difference XRD patterns of the $La_2Ti_2SiO_9$-based solid solutions. Inset shows fragment of the XRD pattern of $LaPrTi_2SiO_9$ after annealing in air at 1323 K for 2 h and quenching in liquid nitrogen.

The structure of single-phase $La_2Ti_2SiO_9$, $LaPrTi_2SiO_{9+\delta}$ and $La_2Ti_{1.8}Nb_{0.2}SiO_{9+\delta}$ was identified as monoclinic, space group $C12/m1$ (n. 12). The refinement, using the starting model from Ref. [28] with 110 fitting

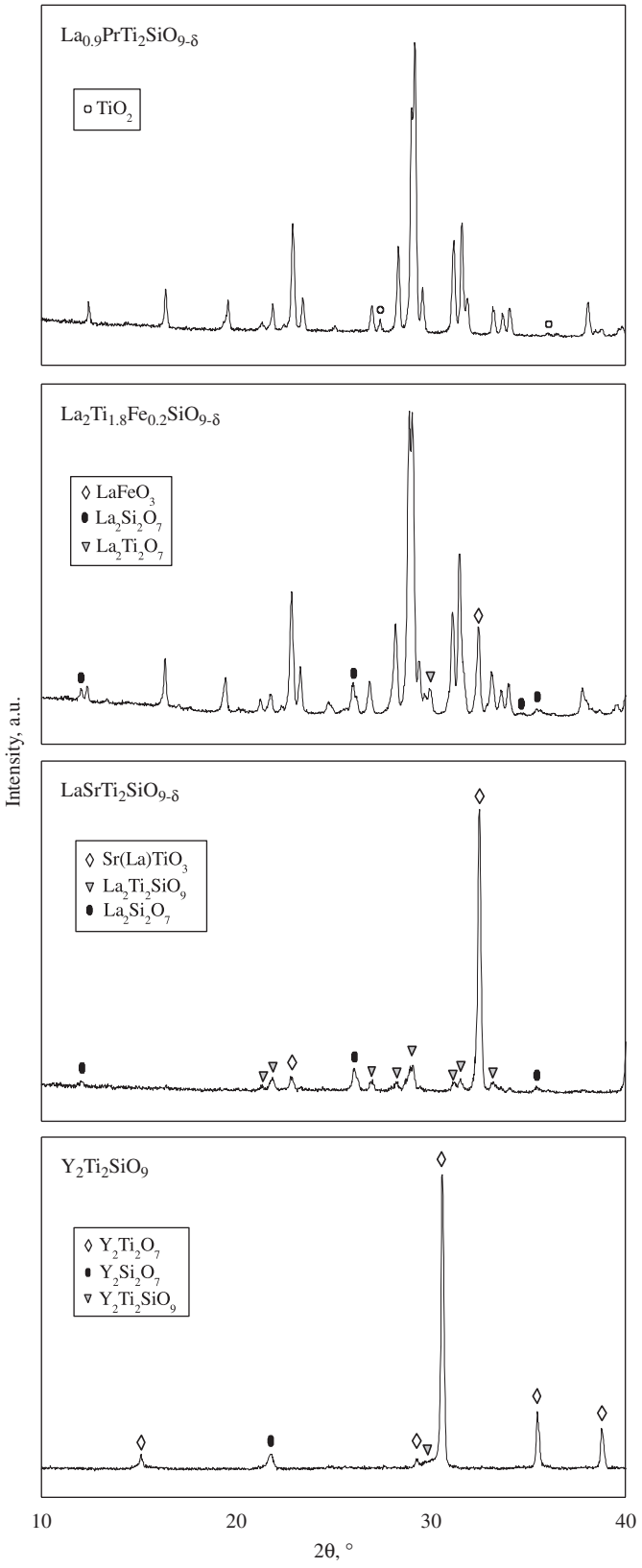

Fig. 3. Fragments of the XRD patterns of $La_2Ti_2SiO_9$-based and $Y_2Ti_2SiO_9$ ceramics.

parameters, provided an excellent agreement between the observed and calculated profiles (Fig. 2). The lattice parameters, agreement factors, atomic coordinates, site occupancies and isotropic thermal parameters are summarized in Tables 1 and 2. The incorporation of $Pr^{3+/4+}$, with a smaller ionic radius if compared to La^{3+} [29], decreases the unit cell volume. An opposite behavior is observed on doping with Nb^{5+}, having a larger size with respect to Ti^{4+}.

Inspection of the structural data (Fig. 2 and Table 2) reveals an absence of cation ordering or tendencies to non-random distribution of Pr and Nb cations between the different sites in the La- and Ti-sublattices, respectively. The calculated cation compositions are very close to nominal, within the limits of experimental error. Due to insufficient sensitivity of XRD method to the lightweight oxygen atoms, no additional oxygen site was considered in the course of refinement of oxygen hyperstoichiometric phase, such as $La_2Ti_{1.8}Nb_{0.2}SiO_{9+\delta}$. In the latter case, however, the presence of extra oxygen in the cavities between adjacent SiO_4 tetrahedra, confirmed by the atomic simulations, results in an apparent increase of the O1 site occupancy up to 1.06(1), Table 2. Another necessary comment is that all compositions exhibit relatively high atomic temperature factors for the tetrahedral O2 oxygen, thus indicating a considerable level of disorder due to SiO_4 relaxations.

The stability of monoclinic $La_2Ti_2SiO_9$-based phases within the studied temperature range, 300–1300 K, was confirmed by the XRD analysis of the samples quenched in liquid nitrogen. The inset in Fig. 2 shows one example, for $LaPrTi_2SiO_{9+\delta}$ annealed at 1323 K for 2 h in air and subsequently quenched. Neither additional peaks nor changes in character of the reflections splitting are observed in the XRD pattern.

3.2. Ceramic microstructure, thermal expansion and total conductivity

The SEM/EDS studies showed a good quality of the prepared ceramics, although minor traces of a glassy phase are visible at the grain boundaries (Fig. 4A–C). Impedance spectroscopy data at temperatures above 850 K showed that the grain-boundary contribution vanished under such circumstances. Typical examples of the impedance spectra are presented in Fig. 5. The specific capacitance of the high-frequency arcs, corresponding to the materials bulk, is in the range 4×10^{-12}–7×10^{-11} F/cm. The low-frequency response, with geometric capacitances of 1×10^{-5}–9×10^{-7} F/cm, is related to the electrode response. The grain-boundary contribution cannot be positively identified in these spectra. It should be mentioned that the observed electrode arcs are relatively small due to a high electronic contribution to the total conductivity [18], in agreement with the EMF and FE data discussed below.

Fig. 6 presents the dilatometric curves of the $La_2Ti_2SiO_9$, $LaPrTi_2SiO_{9+\delta}$ and $La_2Ti_{1.8}Nb_{0.2}SiO_{9+\delta}$ ceramics in air.

Table 1
Rietveld refinement results for monoclinic $La_2Ti_2SiO_9$-based phases (space group $C12/m1$)

Composition	Lattice parameters					Agreement factors	
	a (Å)	b (Å)	c (Å)	β°	V (Å^3)	R_p (%)	R_{wp} (%)
$La_2Ti_2SiO_9$	17.0294(6)	5.7372(2)	7.6385(3)	111.228(2)	695.65(4)	5.44	7.24
$LaPrTi_2SiO_9$	16.9553(3)	5.7263(1)	7.6069(2)	111.348(1)	687.90(2)	5.53	7.14
$La_2Ti_{1.8}Nb_{0.2}SiO_{9.1}$	17.0388(4)	5.7399(1)	7.6426(2)	111.227(1)	696.74(3)	5.09	6.77

Table 2
Structural parameters of $La_2Ti_2SiO_9$-based phases

Composition	Atom	Wyck.	Occ.	x	y	z	Biso
$La_2Ti_2SiO_9$	La1	(4*i*)	1.00(1)	0.2110(1)	0(—)	0.3012(3)	0.87(5)
	La2	(4*i*)	0.99(1)	0.3943(1)	0(—)	0.3012(3)	0.73(5)
	Ti1	(4*g*)	1.00(2)	0.5(—)	0.2562(9)	0(—)	0.93(15)
	Ti2	(4*i*)	0.99(2)	0.4190(4)	0(—)	0.5509(9)	0.99(14)
	Si	(4*i*)	1.01(3)	0.3382(6)	0(—)	0.0185(12)	0.60(20)
	O1	(8*j*)	1.02(4)	0.3798(7)	0.2383(19)	−0.0169(18)	0.59(34)
	O2	(4*i*)	1.00(3)	0.2506(13)	0(—)	0.8716(29)	2.32(39)
	O3	(4*i*)	1.03(5)	0.3465(11)	0(—)	0.2286(24)	0.49(31)
	O4	(8*j*)	1.00(4)	0.3390(9)	0.2394(26)	0.5188(20)	1.02(29)
	O5	(4*i*)	1.01(3)	0.5279(12)	0.5(—)	0.1796(22)	1.44(38)
	O6	(4*h*)	1.01(4)	0.5(—)	0.2071(31)	0.5(—)	059(35)
	O7	(4*i*)	1.02(5)	0.4713(12)	0(—)	0.8180(25)	0.91(36)
$LaPrTi_2SiO_9$	La1/Pr1	(4*i*)	0.43/0.57(3)	0.2109(1)	0(—)	0.3024(2)	0.51(3)
	La2/Pr2	(4*i*)	0.57/0.43(3)	0.3940(1)	0.5(—)	0.3042(2)	0.62(3)
	Ti1	(4*g*)	1.00(2)	0.5(—)	0.2530(6)	0(—)	0.49(9)
	Ti2	(4*i*)	0.99(2)	0.4184(3)	0(—)	0.5501(6)	0.70(8)
	Si	(4*i*)	1.01(3)	0.3378(5)	0(—)	0.0190(9)	0.54(12)
	O1	(8*j*)	1.01(5)	0.3836(5)	0.2414(14)	−0.0163(13)	0.45(21)
	O2	(4*i*)	1.01(4)	0.2540(9)	0(—)	0.8738(22)	2.38(38)
	O3	(4*i*)	1.00(3)	0.3465(8)	0(—)	0.2282(17)	0.58(28)
	O4	(8*j*)	1.01(6)	0.3378(6)	0.2439(18)	0.5191(14)	0.44(19)
	O5	(4*i*)	1.01(3)	0.5257(8)	0.5(—)	0.1816(15)	0.97(31)
	O6	(4*h*)	1.01(4)	0.5(—)	0.2181(23)	0.5(—)	0.38(26)
	O7	(4*i*)	1.01(3)	0.4700(9)	0(—)	0.8109(18)	0.59(26)
$La_2Ti_{1.8}Nb_{0.2}SiO_{9.1}$	La1	(4*i*)	1.00(1)	0.2112(1)	0(—)	0.3015(2)	0.66(5)
	La2	(4*i*)	1.00(1)	0.3944(1)	0.5(—)	0.3041(2)	0.65(6)
	Ti1/Nb1	(4*g*)	0.89/0.11(2)	0.5(—)	0.2551(6)	0(—)	0.85(10)
	Ti2/Nb2	(4*i*)	0.91/0.09(2)	0.4186(3)	0(—)	0.5501(5)	0.80(10)
	Si	(4*i*)	1.00(3)	0.3388(5)	0(—)	0.0193(9)	0.42(15)
	O1	(8*j*)	1.06(2)	0.3832(5)	0.2431(14)	−0.0122(12)	0.73(24)
	O2	(4*i*)	1.00(3)	0.2519(9)	0(—)	0.8755(20)	1.53(33)
	O3	(4*i*)	1.01(4)	0.3433(8)	0(—)	0.2275(17)	0.65(35)
	O4	(8*j*)	1.01(2)	0.3375(6)	0.2405(18)	0.5181(14)	0.79(22)
	O5	(4*i*)	1.00(5)	0.5262(8)	0.5(—)	0.1777(14)	0.80(34)
	O6	(4*h*)	1.00(3)	0.5(—)	0.2259(24)	0.5(—)	0.61(32)
	O7	(4*i*)	1.01(4)	0.4700(9)	0(—)	0.8148(17)	0.51(32)

The average thermal expansion coefficients (TECs) at 300–1373 K vary in the narrow range $(8.7–9.5)\times10^{-6}\,K^{-1}$ (Table 3). These values are close to those of apatite-type silicates [8,9].

In air, at 1100–1300 K, all materials exhibit similar levels of the total conductivity, with the exception of $La_2Ti_{1.8}Nb_{0.2}SiO_{9+\delta}$ having slightly worse electrical properties (Fig. 7). Reducing oxygen partial pressure leads to a substantial increase of the conductivity and a decrease of the activation energies, E_a (Figs. 7 and 8, Table 3). In H_2-containing atmospheres, the maximum conductivity is observed for $LaPrTi_2SiO_{9\pm\delta}$. These changes cannot be attributed to protonic contribution, which seems to become significant only at temperatures below 1000 K as indicated by a further decrease in E_a values, characteristic of the proton conduction. The latter tendency is most

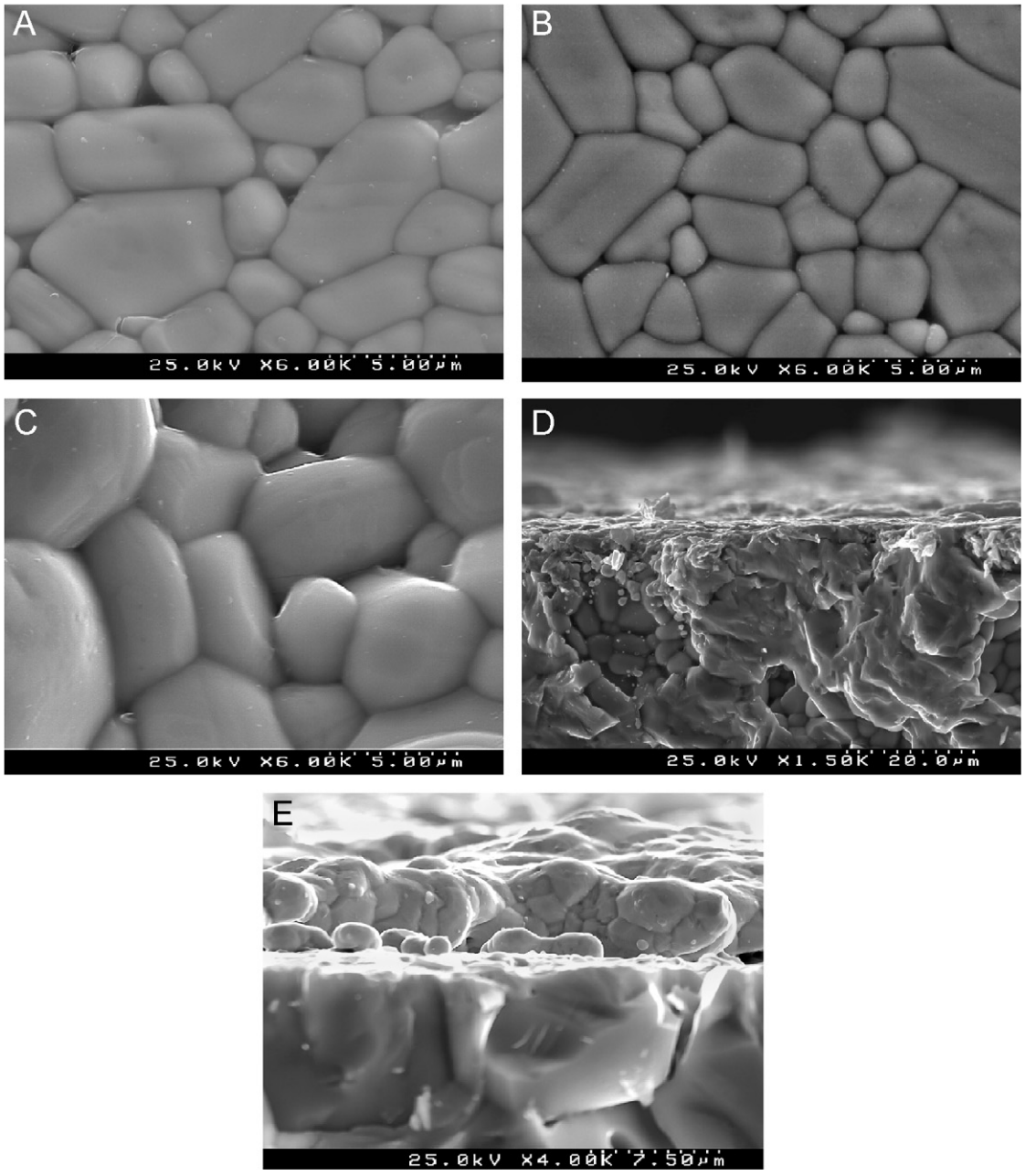

Fig. 4. SEM micrographs of $La_2Ti_2SiO_9$ (A), $LaPrTi_2SiO_9$ (B), $La_2Ti_{1.8}Nb_{0.2}SiO_{9.1}$ (C), H_2-exposed surface of $La_2Ti_2SiO_9$ ceramics after degradation tests (D), and fractured $LaPrTi_2SiO_9$ ceramics with porous Pt layer (top) after the EMF measurements (E).

pronounced for $La_2Ti_2SiO_9$, where the presence of protonic conduction is clearly evidenced by the influence of wet and dry atmospheres on conductivity (Fig. 9). The TGA studies confirm progressive water release from $La_2Ti_2SiO_9$ lattice on heating in dry air (Fig. 10). The room-temperature water content in one $La_2Ti_2SiO_9$ sample equilibrated at $p(H_2O) \approx 0.02$ atm during 6 weeks was estimated as approximately 0.2 molecules per formula unit. Nonetheless, at temperatures above 1100 K the protonic contribution to the total conductivity is negligible even for $La_2Ti_2SiO_9$ (Fig. 9). Therefore, the conductivity increase on reducing oxygen pressure is primarily associated with increasing n-type electronic transport due to the formation of Ti^{3+}. In parallel, formation of oxygen vacancies should also occur. If oxygen vacancies are indeed present and are relevant for the anion diffusion mechanism, the oxygen ionic conductivity should also increase at low $p(O_2)$. This idea will find further support in the remaining discussion on experimental data and modelling results.

A separate comment is necessary on the unusual high-temperature behavior of $LaPrTi_2SiO_{9\pm\delta}$. This material shows substantial weight changes on heating in air, clearly indicating that praseodymium cations are partly tetravalent and reduce when the temperature increases (Fig. 10). On the other hand, the presence of Pr^{4+} has no essential

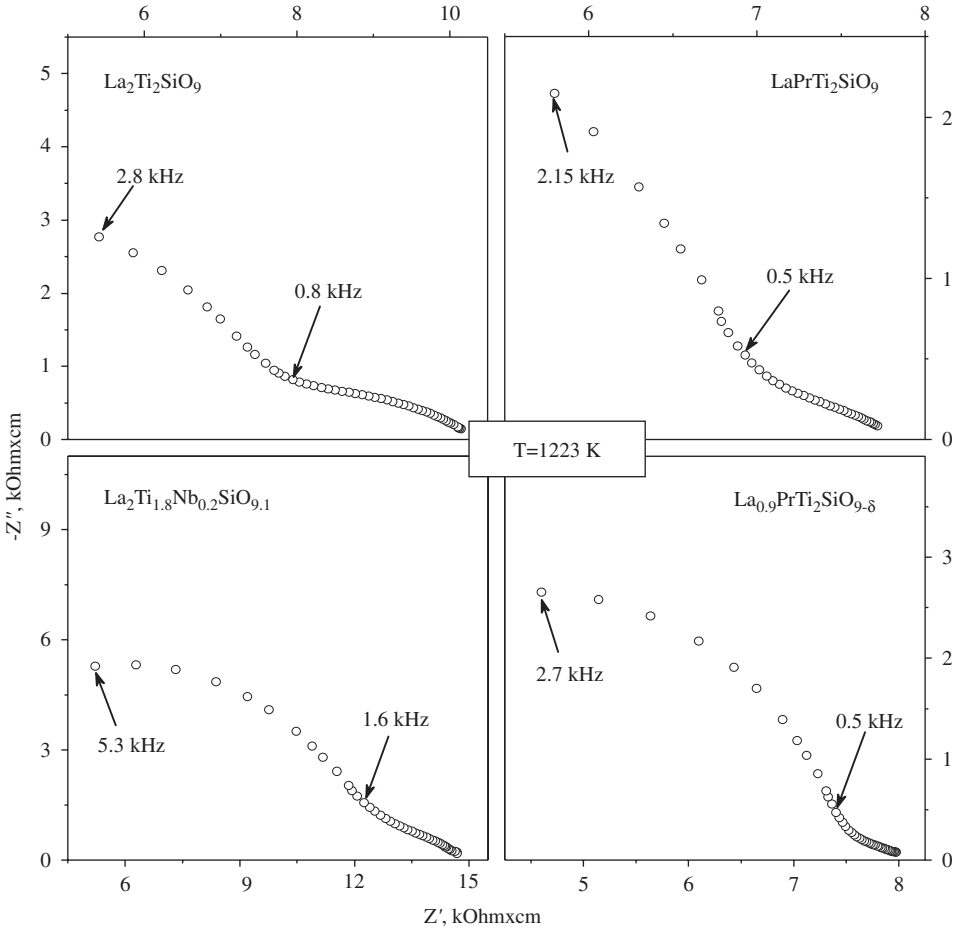

Fig. 5. Examples of the impedance spectra of $La_2Ti_2SiO_9$-based ceramics with porous Pt electrodes, at 1223 K in air.

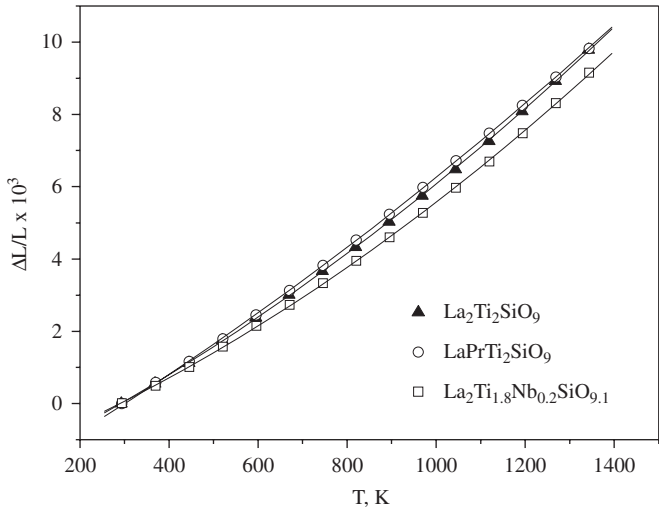

Fig. 6. Dilatometric curves of $La_2Ti_2SiO_9$-based ceramics in air.

effect on the total conductivity (Fig. 7). This suggests that possible contributions of oxygen interstitials and $Pr^{3+/4+}$ redox couple to the ionic and electronic transport are quite small. However, in reducing atmospheres the total conductivity of Pr-containing materials is maximum when compared to the other compositions (Fig. 8). Although the exact reasons for such behavior are not yet fully understood, this effect may hardly be ascribed to the role of grain-boundaries. Only minor segregation of praseodymium-rich phases can be assumed, considering $LaPrTi_2SiO_{9\pm\delta}$ lattice intolerance with respect to *A*-site deficiency. In addition, praseodymium enrichment of the grain boundaries should also lead to the segregation of insulating titanium oxides. It seems, therefore, that the presence of praseodymium has a direct role in defect formation, rather than an indirect microstructural effect. Possible speculations on the mechanism may include increasing tendency for Frenkel-type disorder at low $p(O_2)$/high Pr^{3+} concentration, and/or cooperative shift in Pr^{4+}/Pr^{3+} and Ti^{4+}/Ti^{3+} equilibrium with preferential formation of n-type charge carriers localized in titanium ions.

Finally, Fig. 11 shows the time dependencies of the total conductivity of $La_2Ti_2SiO_9$-based materials in air and in H_2–H_2O–N_2 atmospheres. No degradation is observed. In fact, at low $p(O_2)$ the conductivity tends to increase moderately with time due to slow reduction kinetics. The absence of phase decomposition caused by silicon oxide volatilization in H_2-containing atmospheres was also confirmed by XRD and SEM/EDS. In particular, despite the minor microstructural changes near the ceramics surface exposed to reducing gas (Fig. 4D), the alterations

Table 3
Activation energies for the total conductivity of $La_2Ti_2SiO_9$-based phases in different atmospheres, and thermal expansion coefficients and total conductivity at 973 K in dry air

Composition	E_a (eV)			Average TECs		$\sigma \times 10^6$ (S/cm) (973 K)
	Air	Argon	10%H_2–90%N_2	T (K)	$\bar{\alpha} \times 10^6$(K^{-1})	
$La_2Ti_2SiO_{9\pm\delta}$	1.46±0.07	1.45±0.03	0.83±0.05	300–1373	9.34±0.01	5.3
$LaPrTi_2SiO_{9\pm\delta}$	1.67±0.03	1.62±0.05	1.03±0.28	300–1373	9.47±0.01	3.1
$La_2Ti_{1.8}Nb_{0.2}SiO_{9\pm\delta}$	1.57±0.07	1.48±0.06	0.90±0.10	300–1373	8.71±0.01	2.3

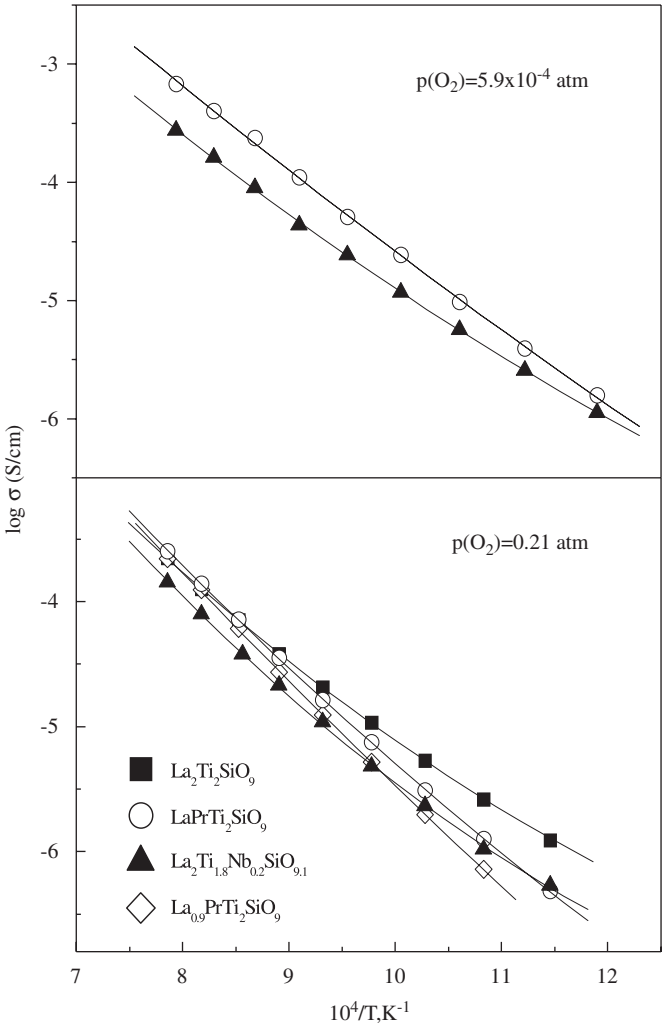

Fig. 7. Temperature dependences of the total conductivity of $La_2Ti_2SiO_9$-based ceramics in dried atmospheric air and Ar–O_2 mixture.

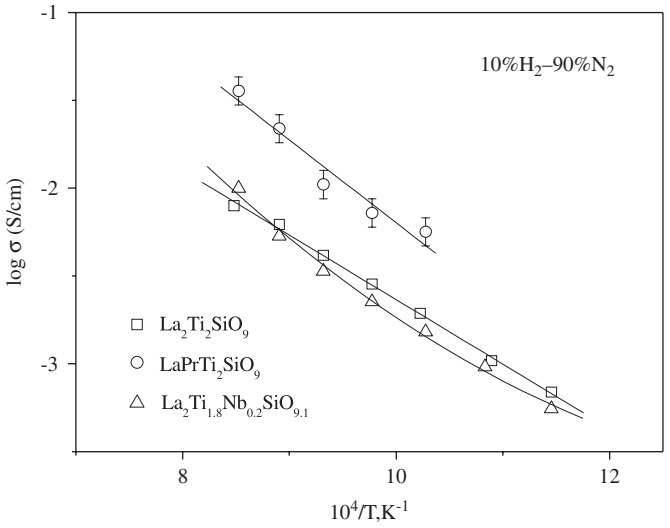

Fig. 8. Temperature dependences of the total conductivity of the $La_2Ti_2SiO_9$-based ceramics in flowing 10%H_2–90%N_2 mixture.

in cation composition evaluated by EDS were found negligible within the limits of experimental uncertainty. The conductivity variations with the oxygen partial pressure, discussed above, are therefore related to the materials bulk.

3.3. Transference numbers and ionic conduction

The EMF and FE studies demonstrated that the conductivity of all studied silicates-titanates is dominated by electronic transport (Table 4). The ion transference numbers (t_o) of $La_2Ti_2SiO_9$ and $La_2Ti_{1.8}Nb_{0.2}SiO_{9.1}$, determined by the EMF method under oxygen/air gradient at 973–1223 K, vary in the range 0.15–0.32. Decreasing oxygen chemical potential leads to a higher ionic contribution to the total conductivity of undoped $La_2Ti_2SiO_9$. An opposite trend is observed for the Nb-containing material. In the case of $LaPrTi_2SiO_{9\pm\delta}$, several attempts to perform EMF measurements failed. The subsequent SEM analysis of platinum electrodes applied onto $LaPrTi_2SiO_{9\pm\delta}$ ceramics, showed strong conglomeration of Pt particles, probably due to surface diffusion of silica. This leads to local deviations from equilibrium chemical potential at the electrodes and to an excessive noise level. The accurate determination of the oxygen ion transference numbers of $LaPrTi_2SiO_{9\pm\delta}$ was only possible with the FE technique [17]. In the latter case, the polarization resistance of Pt electrodes was also relatively high (Fig. 12), but the effects of electrode polarization can be taken into account by combining the Faradaic efficiency and impedance spectroscopy measurements [17]. The oxygen ion transference numbers of $LaPrTi_2SiO_{9\pm\delta}$ at atmospheric oxygen pressure are similar to those of other silicates-titanates, 0.23–0.31 in the temperature range 1098–1223 K.

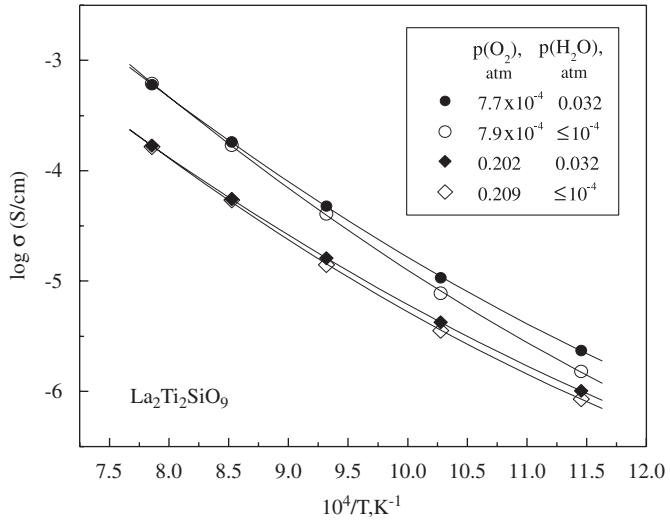

Fig. 9. Temperature dependences of the total conductivity of $La_2Ti_2SiO_{9-\delta}$ ceramics in humidified and dry atmospheres.

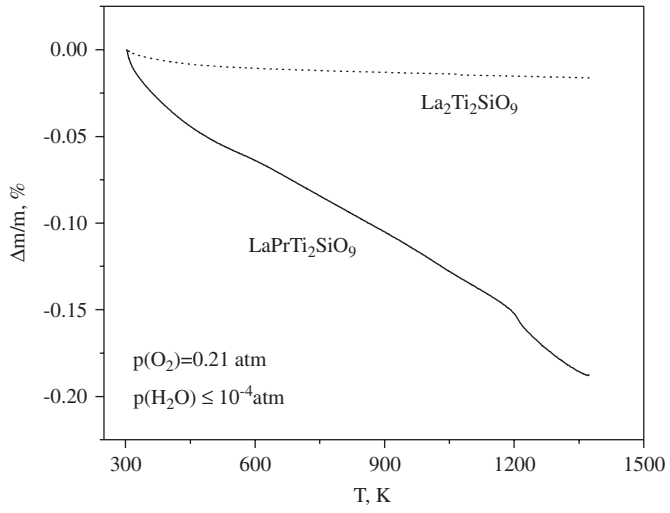

Fig. 10. TGA curves of $La_2Ti_2SiO_9$ and $LaPrTi_2SiO_{9+\delta}$ in dry air.

Fig. 13 compares the partial ionic (σ_o) and electronic (σ_e) conductivities under oxidizing conditions, calculated from the EMF, FE and impedance spectroscopy data. The σ_e values of $La_2Ti_2SiO_9$ and $LaPrTi_2SiO_{9\pm\delta}$ are very similar, confirming that the $Pr^{4+/3+}$ couple direct contribution is negligible. The absence of a network of Pr ions as close neighbors probably prevents the establishment of a hopping mechanism for small polarons. At the same time, the ionic conductivity of this Pr-containing phase is higher, which might indicate a significant role of the oxygen interstitial migration. The same conclusion could be derived from the relatively high activation energy observed for $LaPrTi_2SiO_{9\pm\delta}$ (Table 5). Note that this level of the E_a values for ionic transport is close to that in the cuspidine-type materials [11]. In the case of $La_2Ti_{1.8}Nb_{0.2}SiO_{9\pm\delta}$, the ionic and electronic conductivities are both lower than those of the parent composition. These trends indicate that the electronic transport is primarily governed by the

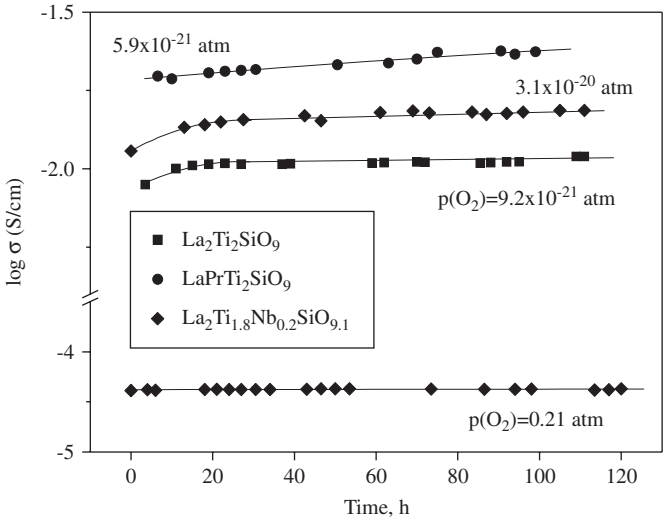

Fig. 11. Time dependences of the total conductivity of the $La_2Ti_2SiO_9$-based materials in flowing air and 10%H_2–90%N_2 mixture at 1173 K. The numbers correspond to the oxygen partial pressure measured by an electrochemical YSZ sensor.

titanium cations, and that the strong coulombic attraction forces between Nb^{5+} and neighboring anions may hamper oxygen migration. The latter hypothesis was validated by the static lattice simulations.

3.4. Atomistic modelling

The difference between simulated lattice parameters and bond distances of $La_2Ti_2SiO_9$, $LaPrTi_2SiO_9$ and $La_2Ti_{1.8}Nb_{0.2}SiO_{9.1}$ and the corresponding experimental values (Tables 1 and 2) was lower than 5%, confirming the quality of potential values used for the computer simulation studies. Also, the modelling results confirmed that incorporation of Pr^{3+} in $La_2Ti_2SiO_9$ is energetic favorable in comparison to Nb^{5+} cations. In the case of Pr^{3+} ions, the solution process was found highly favorable, with the energy of -0.54 eV. For Nb^{5+}, the solution energy was $+0.98$ eV.

The analysis of uncompensated defect formation energies revealed that oxygen vacancies should preferably occupy the O4 positions in the Ti2–O octahedra (Fig. 14A), with a defect energy of 20.26 eV. Attempts to re-locate the vacancies in other oxygen sites, particularly between the two edge-sharing Ti1–O and Ti2–O octahedral, resulted in much higher energies (>22.2 eV). The energetically favorable location of oxygen interstitials was found in the cavities surrounded by SiO_4 tetrahedra and TiO_6 octahedra (Fig. 14B). Note that these estimates of uncompensated defect energies are compatible with literature data [23,30,31]. Their high magnitude results from the contributions related to the formation of free oxygen atoms and the incorporation of charged point defects ignoring electroneutrality.

In order to identify the likely migration path, an O^{2-} anion was firmly placed (using the *fix* option in the GULP

Table 4
Oxygen ion transference numbers determined by EMF and FE methods

Composition	Method	T (K)	$p(O_2)$ (atm)	t_o
$La_2Ti_2SiO_{9\pm\delta}$	EMF	1223	1.0/0.21	0.16
		1173	1.0/0.21	0.19
		1123	1.0/0.21	0.21
		1223	$0.21/1\times10^{-4}$	0.09
		1173	$0.21/8\times10^{-5}$	0.13
		1123	$0.21/8\times10^{-5}$	0.17
		1073	$0.21/7\times10^{-5}$	0.20
		1223	$0.21/8\times10^{-19}$	0.20
		1173	$0.21/8\times10^{-20}$	0.29
		1073	$0.21/6\times10^{-22}$	0.32
$La_2Ti_{1.8}Nb_{0.2}SiO_{9\pm\delta}$	EMF	1223	1.0/0.21	0.15
		1173	1.0/0.21	0.16
		1123	1.0/0.21	0.17
		1073	1.0/0.21	0.22
		1023	1.0/0.21	0.24
		973	1.0/0.21	0.32
		1123	$0.21/2\times10^{-4}$	0.08
		1023	$0.21/1\times10^{-4}$	0.11
		1073	$0.21/2\times10^{-22}$	0.10
		973	$0.21/1\times10^{-23}$	0.12
$LaPrTi_2SiO_{9\pm\delta}$	FE	1223	0.21	0.23
		1148	0.21	0.28
		1098	0.21	0.31

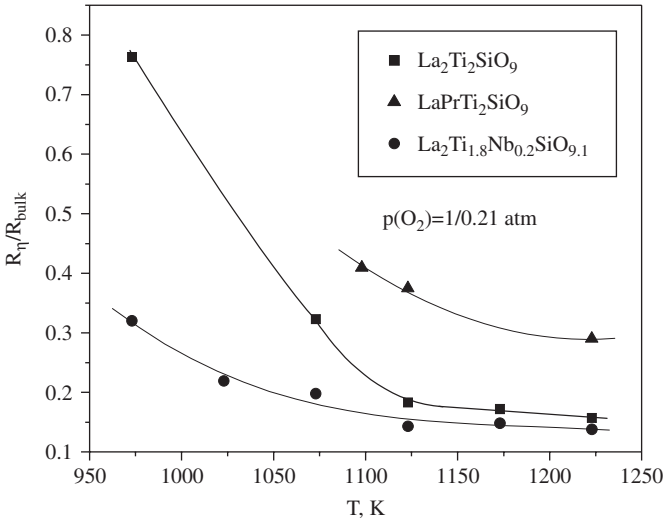

Fig. 12. Temperature dependence of the electrode and bulk resistance ratio, calculated from the EMF and FE data combined with the impedance spectroscopy. The experimental techniques and formulae, used for the calculations, are described in Refs. [17,18].

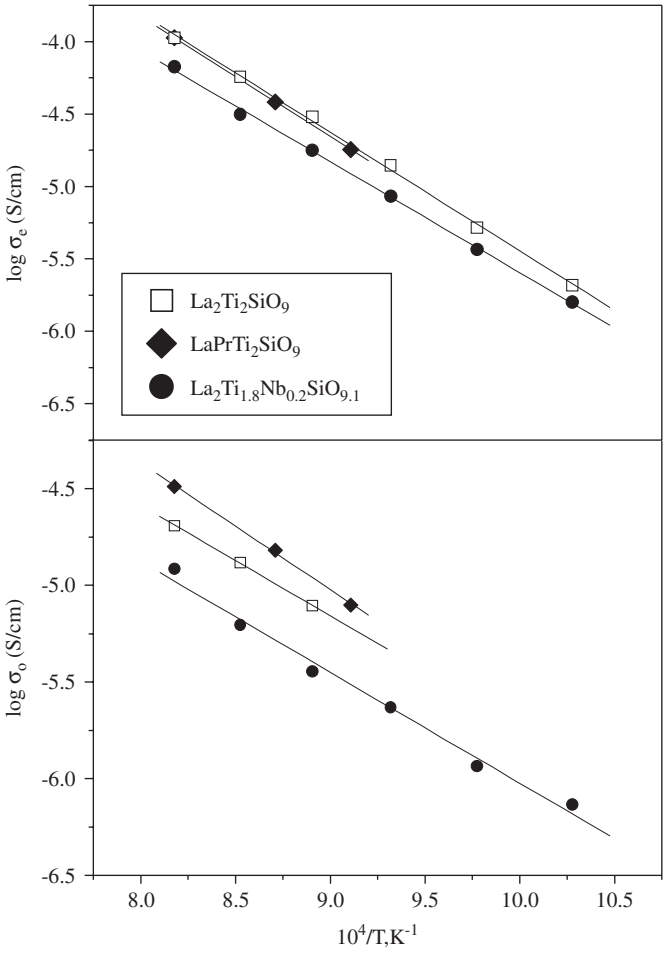

Fig. 13. Temperature dependences of the partial conductivities of the $La_2Ti_2SiO_9$-based materials in air.

Table 5
Activation energy for the partial conductivities in air

Composition	Activation energies (eV)	
	Ionic transport	Electronic transport
$La_2Ti_2SiO_9$	1.23 ± 0.05	1.59 ± 0.05
$LaPrTi_2SiO_{9+\delta}$	1.40 ± 0.12	1.74 ± 0.01
$La_2Ti_{1.8}Nb_{0.2}SiO_{9+\delta}$	1.23 ± 0.05	1.62 ± 0.07

software [19]) at various positions along each hypothetical migration pathway and the energies, after relaxing to zero force, were calculated. The migration energy was defined as the difference between the highest energy position (saddle-point) on a given trajectory and the defect energy in the corresponding equilibrium state. For $La_2Ti_2SiO_9$, preliminary calculations showed that the ionic transport is essentially one-dimensional and may only occur in the layer formed by TiO_6 octahedra and lanthanum cations (Fig. 1), with the overall direction parallel to the b axis. All possible diffusion pathways are strongly nonlinear and consist of several elementary jumps in the directions close to the a and b axes; any diagonal transport was restricted by the high integral migration energies. Fig. 14 shows two possible migration pathways parallel to the b axis, each comprising several elementary steps. These pathways include vacancy jumps between two adjacent TiO_6 octahedra along the [010] and [100] directions, and interstitial jumps between the O_{I1} and O_{I2} positions. The direct jump between the two distant octahedra along the b axis (e.g. between the $O4_{218}$ and $O4_{256}$ sites) was found restricted by

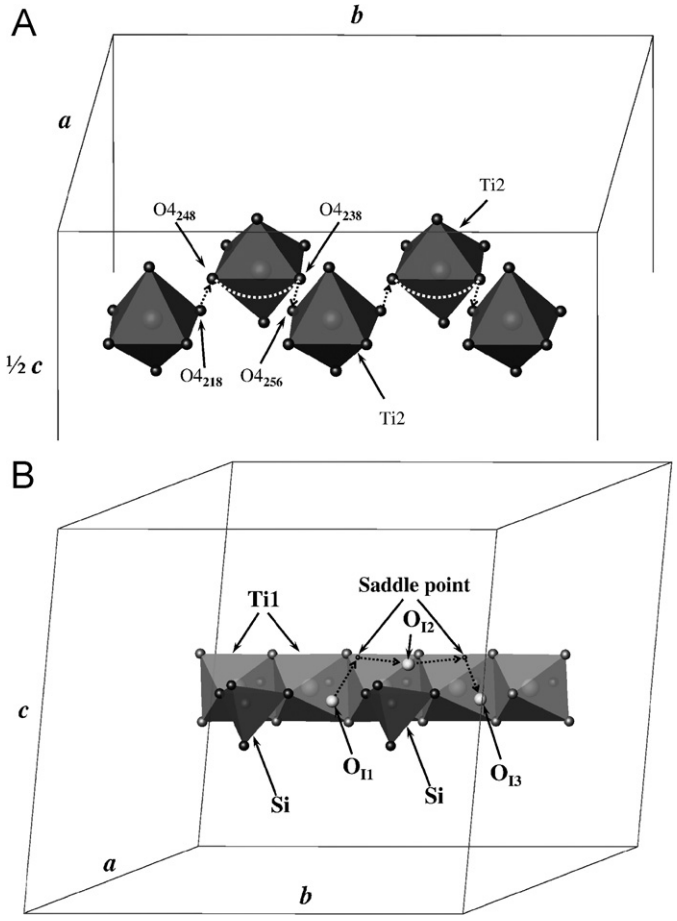

Fig. 14. Migration pathways of oxygen vacancies (A) and oxygen interstitials (B) in $La_2Ti_2SiO_9$ lattice, determined by the atomistic computer simulation technique. Solid lines show the supercell used for modeling.

high migration energies (Table 6), although similar elementary jumps along the *a* axis are possible. The anions can thus migrate along a straight line between the $O4_{218}$ and $O4_{248}$ vacancies with a saddle point situated in the middle of the pathway. The next jump may take place between the $O4_{248}$ and $O4_{238}$ sites (Fig. 14A). Contrary to $O4_{218}$–$O4_{248}$ transfer, the latter jump should occur via a curved trajectory, with the saddle point located under the *a*–*b* plane of TiO_6 octahedra at a distance of 0.66 Å from the midpoint of the octahedron edge; similar non-linear pathways are known for perovskite-type lattices [30]. The interstitial migration also occurs via a non-linear trajectory; the saddle point is above the edge of TiO_6 octahedra (Fig. 14B).

The qualitative conclusions drawn for $La_2Ti_2SiO_9$ are also valid for $LaPrTi_2SiO_9$, with a modest difference in the stereological and energetic parameters. In the case of $La_2Ti_{1.8}Nb_{0.2}SiO_{9.1}$, the ion diffusion mechanism becomes more complex. As expected, the higher effective charge of Nb^{5+} with respect to Ti^{4+} leads to trapping of neighboring anions, particularly in the O_{I1} interstitial and $O4_{256}$ regular positions (Fig. 14). Although the average migration energies remain similar to other compositions, the anions

Table 6
Calculated defect migration energies in $La_2Ti_2SiO_9$-based lattices

Composition	Mechanism	Starting position of O^{2-} ion	Final position of O^{2-} ion	E_m (eV)
$La_2Ti_2SiO_9$	Vacancy	$O4_{218}$	$O4_{248}$	2.32
	Vacancy	$O4_{248}$	$O4_{238}$	1.50
	Vacancy	$O4_{238}$	$O4_{256}$	2.32
	Vacancy	$O4_{218}$	$O4_{256}$	3.20
	Interstitial	O_{I1}	O_{I2}	2.20
	Interstitial	O_{I2}	O_{I1}	2.20
$LaPrTi_2SiO_9$	Vacancy	$O4_{218}$	$O4_{248}$	2.48
	Vacancy	$O4_{248}$	$O4_{238}$	1.90
	Vacancy	$O4_{238}$	$O4_{256}$	2.33
$La2Ti_{1.8}Nb_{0.2}SiO_{9.1}$	Vacancy	$O4_{218}$	$O4_{248}$	2.36
	Vacancy	$O4_{248}$	$O4_{238}$	1.62
	Vacancy	$O4_{238}$	$O4_{256}$	1.91
	Vacancy	$O4_{256}$	$O4_{238}$	2.82
	Interstitial	O_{I2}	O_{I1}	1.73
	Interstitial	O_{I1}	O_{I2}	2.91

migrating via the $O4_{256}$–$O4_{238}$ regular sites and O_{I1}–O_{I2} interstitial positions should overcome an additional potential barrier, 0.9–1.2 eV, when Nb^{5+} cations are present in the vicinity of diffusion path. This is reflected by anisotropic migration energies (Table 6). The oxygen anions near Nb^{5+} appear thus blocked, resulting in a lower concentration of the ionic charge carriers and lower conductivity (Fig. 13). It should also be stressed that the coulombic attraction forces between the Pr^{4+} cations and neighboring anions should be essentially weaker than that for Nb^{5+}, while the distance between praseodymium and nearest oxygen interstitials in $LaPrTi_2SiO_9$ ($\geqslant$2.591 Å) is longer if compared to niobium cations in $La_2Ti_{1.8}Nb_{0.2}SiO_{9.1}$ ($\geqslant$1.905 Å). The anion-trapping effect in the Pr-containing compounds is, hence, considerably lower.

In general, the interstitial diffusion in $La_2Ti_2SiO_9$-based lattices is less favorable, from an energetic point of view, when compared to the vacancy mechanism. Comparison of the experimental E_a values (Table 5) and the calculated migration energies (Table 6), shows that the vacancy transport should prevail. For the oxygen-hyperstoichiometric phases such as $La_2Ti_{1.8}Nb_{0.2}SiO_{9+\delta}$ and $LaPrTi_2SiO_{9+\delta}$, the mobile vacancies may be formed, in particular, due to Frenkel-type disorder. Although the relatively high ionic conductivity of $LaPrTi_2SiO_{9\pm\delta}$ under oxidizing conditions suggests that the role of oxygen interstitial may still be significant, the vacancy migration is expected to completely dominate in reducing atmospheres when Ti^{3+} cations are formed.

3.5. Partial conductivities vs. oxygen pressure

As the electron transference numbers are higher than 0.5 (Table 4), the increase in the total conductivity on reduction (Figs. 7 and 8) unambiguously indicates a predominant role of n-type charge carriers in the electronic

transport processes. At the same time, the conductivity in H_2-containing atmospheres is more than 10 times higher than that under oxidizing conditions, whilst the ion transference numbers remain significant. These changes show that as for the n-type electronic conduction, the ionic transport in reducing environments increases as well, in agreement with the atomistic simulation results. The generation of ionic and n-type electronic charge carriers on reduction can be described by the simplest reaction:

$$O_O^{\times} \rightarrow \frac{1}{2}O_2 + 2e' + V_O^{\bullet\bullet}, \quad (2)$$

where the Kröger-Vink notation [32] is used. In such circumstances, the $p(O_2)$-dependencies of the partial conductivities may be expressed by the empirical model [33]:

$$\sigma_{ion} = K_1 p(O_2)^{1/m} + K_2, \quad (3)$$

$$\sigma_e = K_3 p(O_2)^{1/m} + K_4, \quad (4)$$

where slope m and K_1, K_2, K_3 and K_4 denote the oxygen pressure-independent parameters. In this model, K_2 and K_4 correspond to the values of partial conductivities under strongly oxidizing conditions, where the charge-carrier concentrations are determined by impurity content and/or intrinsic disorder processes and are, thus, $p(O_2)$-independent. The slope m is determined by a defect formation reaction (e.g. Eq. (2)) and the crystal electroneutrality condition in another limiting case, when $p(O_2)^{1/m} \gg K_2$ and $K_3 p(O_2)^{1/m} \gg K_4$. In a classical case where the oxygen-vacancy and electron concentration are exclusively governed by Eq. (2), $1/m$ is equal to $-1/6$. The sums (K_1+K_3) and (K_2+K_4), and the value of m can be estimated analyzing the experimental data on the total conductivity as a function of the oxygen pressure.

The transference numbers obtained by the EMF method are averaged in the given oxygen chemical potential (μ) range:

$$t_o = \frac{1}{\mu_2-\mu_1}\int_{\mu_1}^{\mu_2}\frac{\sigma_{ion}}{\sigma_{ion}+\sigma_e}\,d\mu = \left(\ln\frac{p_2}{p_1}\right)^{-1} \times \int_{p_1}^{p_2}\frac{K_1 p(O_2)^{1/m}+K_2}{(K_1+K_3)p(O_2)^{1/m}+(K_2+K_4)}\frac{1}{p(O_2)}\,dp(O_2), \quad (5)$$

where p_1 and p_2 are the values of oxygen partial pressure at the electrodes. Integration of Eq. (5) yields:

$$t_o = \frac{K_2}{K_2+K_4} + \frac{K_2 m}{(K_2+K_4)\ln\frac{p_2}{p_1}} \times \ln\left(\frac{K_2+K_4+(K_1+K_3)p_1^{1/m}}{K_2+K_4+(K_1+K_3)p_2^{1/m}}\right) + \frac{K_1 m}{(K_1+K_3)\ln\frac{p_2}{p_1}}\ln\left(\frac{K_2+K_4+(K_1+K_3)p_2^{1/m}}{K_2+K_4+(K_1+K_3)p_1^{1/m}}\right). \quad (6)$$

After the substitution of (K_1+K_3), (K_2+K_4) and m, and using the experimental values of t_o, p_1 and p_2 for two $p(O_2)$ gradients, Eq. (6) can be solved for K_1, K_2, K_3 and K_4. These parameters were used to evaluate the partial conductivities under equilibrium conditions (Fig. 15). The calculated $1/m$ values are indeed close to $-1/6$ at

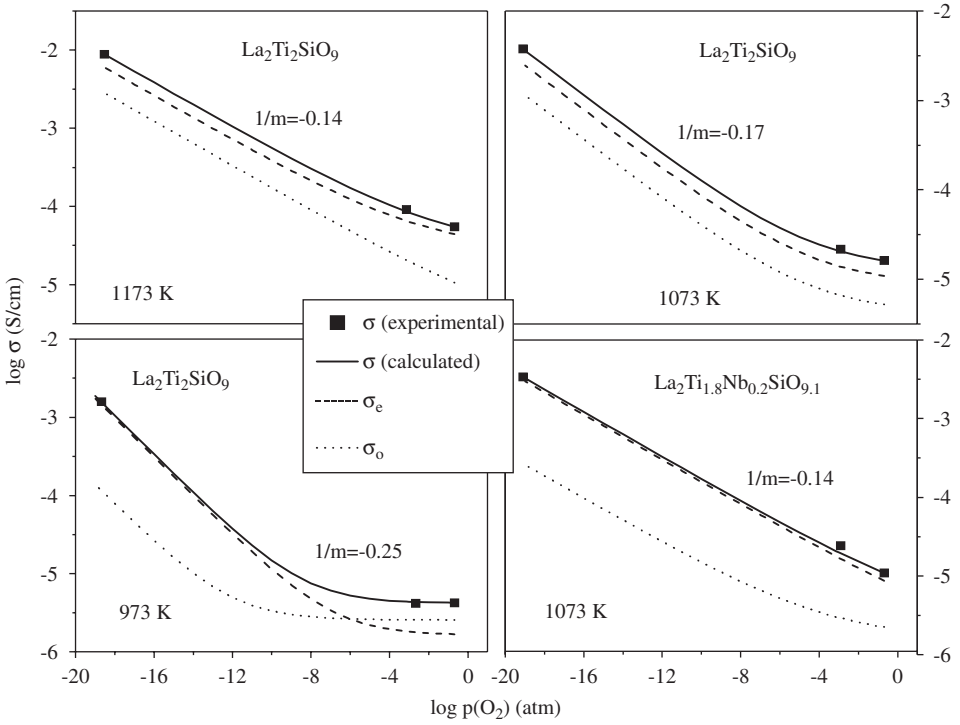

Fig. 15. Oxygen partial pressure dependencies of the partial conductivities of the $La_2Ti_2SiO_9$-based materials, calculated from the total conductivity and EMF data in different atmospheres.

1073–1173 K. At lower temperatures, m tends to decrease, possibly due to an increasing role of protonic transport. Note that the defect association/interaction within such an extended range of working conditions, where the defects concentration is expected to vary about three orders of magnitude, may also lead to deviations from the simple tendencies used in the adopted model. Nonetheless, whatever the defect formation mechanism, the results confirm that the oxygen ionic conduction in reducing atmospheres occurs via the vacancy migration.

4. Conclusions

At 973–1223 K monoclinic $La_2Ti_2SiO_{9\pm\delta}$ exhibits a mixed oxygen-ionic and n-type electronic conductivity, which increases when the oxygen partial pressure is reduced down to 10^{-21} atm. Both conductivity contributions increase due to simultaneous formation of oxygen vacancies and Ti^{3+}. The protonic contribution in wet atmospheres becomes significant at temperatures below 1000 K. The oxygen ion transference numbers of $La_2Ti_2SiO_{9-\delta}$, $LaPrTi_2SiO_{9\pm\delta}$ and $La_2Ti_{1.8}Nb_{0.2}SiO_{9+\delta}$ ceramics, measured by the modified faradaic efficiency and e.m.f. methods accounting for electrode polarization, vary in the range 0.15–0.32. In air, the activation energies for the ionic and electronic transport are 1.23–1.40 and 1.59–1.74 eV, respectively. Doping with praseodymium increases both contributions to the total conductivity, whereas the substitution of Ti^{4+} with Nb^{5+} has opposite effects. The transport properties of $La_2Ti_2SiO_9$-based phases and the atomistic modelling results suggest that oxygen ionic conduction is primarily governed by the defect-formation and diffusion processes involving the TiO_6 octahedra. The ionic transport is essentially one-dimensional and occurs in the direction parallel to the b axis of $La_2Ti_2SiO_9$ lattice. Although the migration of interstitial oxygen surrounded by relaxing SiO_4 octahedra and TiO_6 octahedra may also play an important role, the vacancy mechanism seems dominant, at least in reducing atmospheres. The thermal expansion coefficients of these ceramics, in the range $(8.7–9.5)\times10^{-6}\,K^{-1}$ at 300–1373 K, are similar to those of apatite-type silicates. The $La_2Ti_2SiO_9$ lattice tolerance with respect to A-site deficiency and doping with lower-valence cations, such as Sr and Fe, is much lower than that of the apatite phases, limiting for the role of compositional optimization.

Acknowledgments

This work was partially supported by the FCT, Portugal (POCI program), the European Network of Excellence FAME, and the MatSILC project (STRP 033410, CEC). The authors are sincerely grateful to A.L. Shaula for helpful discussions and experimental assistance.

References

[1] B.C.H. Steele, J. Mater. Sci. 36 (2001) 1053.
[2] O. Yamamoto, Electrochem. Acta 45 (2000) 2423.
[3] S. Nakayama, T. Kageyama, H. Aono, Y. Sadaoka, J. Mater. Chem. 5 (1995) 1801.
[4] S. Nakayama, M. Highchi, J. Mater. Sci. Lett. 13 (2001) 913.
[5] E.J. Abram, D.C. Sinclair, A.R. West, J. Mater. Chem. 11 (2001) 1978.
[6] V.V. Kharton, A.L. Shaula, M.V. Patrakeev, J.C. Waerenborgh, D.P. Rojas, N.P. Vyshatko, E.V. Tsipis, A.A. Yaremchenko, F.M.B. Marques, J. Electrochem. Soc. 151 (2004) A1236.
[7] P.R. Slater, J.E.H. Sansom, Solid State Phenom. 90–91 (2003) 195.
[8] A.L. Shaula, V.V. Kharton, F.M.B. Marques, J. Solid State Chem. 178 (2005) 2050.
[9] V.V. Kharton, A.L. Shaula, M.V. Patrakeev, J.C. Waerenborgh, D.P. Rojas, N.P. Vyshatko, E.V. Tsipis, A.A. Yaremchenko, F.M.B. Marques, J. Electrochem. Soc. 151 (2004) A1236.
[10] O. Joubert, A. Magres, A. Chesnaud, M.T. Caldes, V. Jayarman, Y. Piffard, L. Brohan, Solid State Sci. 4 (2002) 1413.
[11] M.C. Martin-Sodeno, D. Marrero-Lopez, E.R. Losilla, S. Bruque, P. Nunez, M.A.G. Aranda, J. Solid State Chem. 179 (2006) 3445.
[12] B.C.H. Steele, A. Heinzel, Nature 414 (2004) 345.
[13] N.Q. Minh, Solid State Ionics 174 (2004) 271.
[14] A. Bieberle, L.J. Gauckler, in: H.L. Tuller, J. Schoonman, I. Riess (Eds.), Oxygen Ion and Mixed conductors and Their Technological Applications, Kluwer, Dortrecht-Boston-London, 2000, p. 389.
[15] C. Lara, M.J. Pascual, A. Durán, Bol. Soc. Esp. Ceram. Vidrio 42 (2003) 133.
[16] Rodriguez-Carvajal, Physica B 192 (1993) 55.
[17] V.V. Kharton, A.L. Shaula, N.P. Vyshatko, F.M.B. Marques, Electrochim. Acta 48 (2003) 1817.
[18] V.V. Kharton, F.M.B. Marques, Solid State Ionics 140 (2001) 381.
[19] J.D. Gale, J. Chem. Soc. Faraday Trans. 97 (1997) 33.
[20] C.R.A. Catlow, in: W.C. Mckrodt (Ed.), Computer Simulation of Solids, Springer, Berlin, 1982.
[21] B.G. Dick, A.W. Overhauser, Phys. Rev. 112 (1958) 90.
[22] N.F. Mott, M.J. Littleton, Trans. Faraday Soc. 34 (1938) 485.
[23] J.R. Tolchard, M.S. Islam, P.R. Slater, J. Mater. Chem. 13 (2003) 1956.
[24] T.S. Bush, J.D. Gale, C.R.A. Catlow, P.D. Battle, J. Mater Chem. 4 (1994) 831.
[25] R.C. Baetzold, Phys Rev. B 48 (2003) 5789.
[26] C.R.A. Catlow, Computer Modelling in Inorganic Crystallography, Academic Press, San Diego, 1997.
[27] U. Kolitsch, Eur. J. Miner. 13 (2001) 761.
[28] D. Benbertal, A. Mosset, J.C. Trombe, Mater. Res. Bull. 29 (1994) 47.
[29] R.D. Shannon, Acta Crystallogr. A 32 (1976) 751.
[30] G.C. Mather, M.S. Islam, Chem. Mater. 17 (2005) 1736.
[31] C.A.J. Fisher, M.S. Islam, J. Mater. Chem. 15 (2005) 3200.
[32] F.A. Kröger, The Chemistry of the Imperfect crystals, North-Holland, Amsterdam, 1974.
[33] E.V. Tsipis, C.N. Munnings, V.V. Kharton, S.J. Skinner, J.R. Frade, Solid State Ionics 177 (2006) 1015.